RESEARCH ARTICLE | JANUARY 05 2026

Droplet dynamics across a hydrophobic to hydrophilic chemical step

Sacha B. Szkudlarek ; Orest Shardt ; Chris R. Kleijn ; Bijoy Bera

Appl. Phys. Lett. 128, 012701 (2026)
https://doi.org/10.1063/5.0308251

Applied Physics Letters ARTICLE pubs.aip.org/aip/apl

Droplet dynamics across a hydrophobic to hydrophilic chemical step

Cite as: Appl. Phys. Lett. **128**, 012701 (2026); doi: 10.1063/5.0308251
Submitted: 21 October 2025 · Accepted: 16 December 2025 ·
Published Online: 5 January 2026

Sacha B. Szkudlarek,[1] Orest Shardt,[2] Chris R. Kleijn,[3] and Bijoy Bera[1,a)]

AFFILIATIONS

[1]Interfacial Physics Lab, Faculty of Applied Science, Delft University of Technology, Delft 2629HZ, The Netherlands
[2]Bernal Institute and Department of Chemical Sciences, Faculty of Science and Engineering, University of Limerick, Limerick V94 T9PX, Ireland
[3]Transport Phenomena Section, Faculty of Applied Science, Delft University of Technology, Delft 2629HZ, The Netherlands

[a)]Author to whom correspondence should be addressed: b.bera-1@tudelft.nl

ABSTRACT

The dynamics of a droplet on an inclined plane containing a chemical step, implying a heterogeneity in the wettability, have been widely studied because of their relevance to many applications. However, the modeling of such dynamics remains inaccurate due to the lack of implementation of contact angle hysteresis. In this work, we implement a chemical potential wetting boundary condition that includes hysteresis in a well-balanced lattice Boltzmann simulation to address that specific shortcoming. We investigate the behavior of droplet dynamics including this hysteresis force, and subsequently, also probe the effects of chemical step strength, inclination angle, and droplet volume on the droplet dynamics. We observe that the dynamics at the leading and the trailing edges of the droplet are significantly impacted by hysteresis effects and the chemical step strength. In addition, we conclude that for varying inclination angles, the hysteresis contribution is comparable to other contributing forces in the precise manipulation of the droplet.

In daily life and industrial applications,[1–9] liquid droplets commonly move on a solid substrate, while the whole system is submerged in a third liquid/fluid phase. This phenomenon can occur on multiple length scales: ranging from sub-micrometer channels and micrometer bubbles in electrolyzers to millimeter rain droplets on lotus leaves and meter-scale hydrogen storage. While droplets moving on a homogeneous substrate have been studied extensively,[10,11] the last few decades have seen a focus on patterned surfaces, in an attempt to mimic nature, for example, a self-cleaning lotus leaf.[12] The complex interplay of the three-phase contact line with the physical structures and the impact of such interplay on the overall system statics and dynamics have also been studied in detail.[1–9,13–16]

More recently, in addition to physical heterogeneities, chemical patterns have gained widespread attention. Chemical patterns arise naturally or are engineered to control droplet motion in applications such as dew harvesting[1–6,16] and microfluidic devices.[7–9] In tandem with experimental studies, numerical investigations have explored droplet dynamics on chemically patterned substrates. Initial studies have focused more on the trapping of the droplet at the wetting defect.[17] Subsequently, researchers investigated the shape of such a trapped droplet, either by force balance[18] or by energy minimization.[19] Recently, researchers numerically investigated the dynamics of a droplet moving from a hydrophilic to a hydrophobic region on a substrate, i.e., a chemical step impeding droplet motion.[20] These studies found that both the motion and (possible) trapping of the droplet are influenced by the angle of inclination and the strength of the chemical step (i.e., the difference in contact angle between the hydrophilic and the hydrophobic parts). However, one significant omission in the investigation of droplet dynamics on an inclined chemical step is accelerated motion due to a hydrophobic to hydrophilic transition, even though this chemical step occurs frequently in several processes. For example, in an electrolyzer, gas bubbles form at a hydrophobic site and subsequently move up the inclined electrode by displacing water from hydrophilic regions. Another missing link is the inclusion of contact angle hysteresis (CAH), despite the knowledge that removing CAH from the model leads to predictions that conflict with experiments.[17]

In this work, we numerically investigate the dynamics of a droplet on an inclined substrate where the droplet descends from an upper hydrophobic region over a chemical step to a lower hydrophilic region. Figure 1 shows the example under consideration. The example reflects

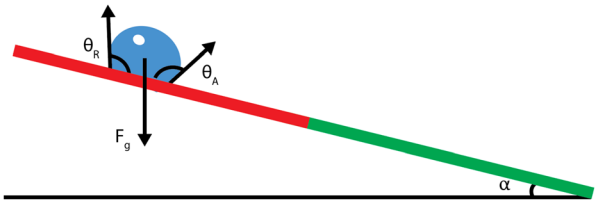

FIG. 1. Schematic of a chemical step. The substrate is divided into a hydrophobic region (red) and a hydrophilic region (green), indicating a step change in the contact angle. Here, F_g (arrow) is the applied gravitational force, and α is the inclination angle of the substrate.

a low-density ratio case, e.g., a water droplet moving on a substrate submerged in oil. We combine a well-balanced free-energy lattice Boltzmann method (WB-LBM)[21] with a chemical potential wetting boundary condition[22,23] that implements CAH.[24,25] This sheds light on the nature of the dynamics at the leading and trailing edges of the droplet. Subsequently, we also consider the effect of the inclination angle, step strength, and droplet volume on the motion of the droplet over the chemical step.

The motion of the fluid is described by the Navier–Stokes equations. The continuity equation governs mass conservation,

$$\partial_t \rho + \nabla \cdot (\rho \vec{v}) = 0, \tag{1}$$

where ρ and $\vec{v}$ are the fluid density and velocity, while momentum conservation is described by

$$\partial_t (\rho \vec{v}) + \nabla \cdot (\rho \vec{v}\vec{v}) = \nabla \cdot \overleftrightarrow{\sigma'} + \vec{f}, \tag{2}$$

where $\overleftrightarrow{\sigma'} = \mu(\nabla \vec{u} + \nabla \vec{u}^T - \frac{2}{3}(\nabla \cdot \vec{u})I)$ is the stress tensor, μ is the dynamic viscosity, and $\vec{f} = \vec{f}_{\text{ext}} + \vec{f}_{\text{int}}$ represents the external and internal force densities that act on the fluid, where in this work, $\vec{f}_{\text{ext}}$ is the gravity. The free energy of the system is used to describe the multiphase behavior, which enters Eq. (2) through the interaction force ($\vec{f}_{\text{int}}$). In this work, a double-well free energy has been implemented.[21]

The addition of interaction forces to conventional LBM results in a discrete force imbalance, leading to the introduction of the well-balanced LBM (WB-LBM).[21] The WB-LBM with the Bhatnagar–Gross–Krook (BGK) collision operator[26] and the two-dimensional nine-velocity (D2Q9) discretization are employed. The evolution of population distributions $h_i(\vec{x}, t)$ is expressed as

$$\begin{aligned} &h_i(\vec{x} + \vec{c}_i \Delta t, t + \Delta t) - h_i(\vec{x}, t) \\ &= \frac{1}{\tau}(h_i(\vec{x}, t) - h_i^{eq}(\vec{x}, t)) + \Delta t \left(1 - \frac{1}{2\tau}\right) S_i, \end{aligned} \tag{3}$$

where $h_i^{eq}(\vec{x}, t)$ is the equilibrium distribution function, at position $\vec{x}$ and time t, τ is the dimensionless relaxation time, and $\vec{c}_i$ represents the discrete velocities of the D2Q9 model,[27] as specified in the supplementary material. The equilibrium distribution function is given by[28]

$$h_i^{eq} = \begin{cases} \rho + w_0 \rho s_0(\vec{u}) & \text{if } i = 0, \\ w_i \rho s_i(\vec{u}) & \text{if } i \neq 0, \end{cases} \tag{4}$$

where $s_i(\vec{u}) = \frac{c_{i\alpha} u_\alpha}{c_s^2} + \frac{u_\alpha u_\beta (c_{i\alpha} c_{i\beta} - c_s^2 \delta_{\alpha\beta})}{2c_s^4}$, $\vec{u}$ is the velocity, ρ is the density, w_i is the weight coefficient for each velocity direction, and c_s represents the lattice speed of sound. Finally, the source term in Eq. (3) Droplet dynamics across a hydrophobic to hydrophilic chemical step is given by[28]

$$S_i = w_i \left[\frac{c_{i\alpha} f_\alpha}{c_s^2} + \frac{u_\beta (f_\alpha + c_s^2 \partial_\alpha \rho)(c_{i\alpha} c_{i\beta} - c_s^2 \delta_{\alpha\beta})}{c_s^4} + \frac{1}{2}\left(\frac{c_i^2}{c_s^2} - D\right) u_k \partial_k \rho \right], \tag{5}$$

where summation over repeated indices is implied, $\delta_{\alpha\beta}$ is the Kronecker delta, D is the spatial dimension (2 in our simulation), and F_α represents the components of $\vec{f}$ from Eq. (2). It is possible to implement the forces from Eq. (2) in the WB-LBM by substituting $\vec{f} = \vec{f}_{\text{int}} + \vec{f}_g$ into Eq. (5) Droplet dynamics across a hydrophobic to hydrophilic chemical step, where $\vec{f}_{\text{int}} = -\rho \vec{\nabla} \mu$ and $\vec{f}_g = \rho \vec{g}$, where ρ is the density, μ is the chemical potential, and $\vec{g}$ is the gravitational acceleration. More details on the derivation of the chemical potential (μ) can be found in the supplementary material. Through the Chapman–Enskog expansion of the WB-LBM, Eqs. (1) and (2) are recovered.[21]

A chemical potential–based wetting boundary condition is employed, based on the approach presented by Yu *et al.*[22] The chemical potential at the boundary between the fluid and the solid is determined based on the desired wetting properties. This approach ensures that the chemical potential at the boundary is compatible with the fluid domain and maintains thermodynamic consistency, unlike traditional wetting boundary implementations.[29,30] To calculate the contact angle, the location of the interface is determined through linear interpolation between the lattice nodes adjacent to the interface.[23] The contact angle is determined by considering the angle made with the surface by the line connecting interface positions at the second and the third layer of lattice nodes. This eliminates boundary layer distortions, which previously resulted in errors in the hydrophilic regimes.[23] Finally, CAH is a crucial part of the wetting dynamics. Our implementation of CAH is inspired by the variable solid–fluid interaction strength approach implementing a static CAH window ($[\theta_A, \theta_R]$),[24,25] adapted to the free energy WB-LBM and the chemical potential boundary condition.

A schematic of the simulation domain (401 × 101 lattice units) is shown in Fig. 2. The system consists of an aqueous droplet sliding down an inclined substrate submerged in a non-aqueous surrounding liquid. The surrounding phase has a density equal to one-third of the dispersed phase. In principle, the WB-LBM employed here can be extended to high-density-ratio (water–air) systems, but such cases are not investigated in this work. Gravity serves as the driving force, depicted in Fig. 1, with its component along the incline given by $F_{g,x} = \int_V \vec{f}_g \sin(\alpha) = mg \sin(\alpha)$, where $\vec{f_g}$ is the gravitational force density, α is the inclination angle, m is the mass of the droplet, and g is the gravitational acceleration. The droplet deforms as it moves at moderate Bond numbers ($\text{Bo} \equiv \frac{\Delta \rho g L^2}{\gamma} = 0.1$–$1$, where $\Delta\rho$ is the density difference, g is the gravitational acceleration, L is the characteristic length scale (droplet base radius R_0), and γ is the interfacial tension between the two liquid phases), resulting in advancing (θ_A) and receding (θ_R) contact angles due to contact angle hysteresis (CAH). These wetting characteristics are implemented through the adapted boundary conditions. At the chemical step, the leading edge contact angle decreases due to the difference in wetting conditions until it falls within the

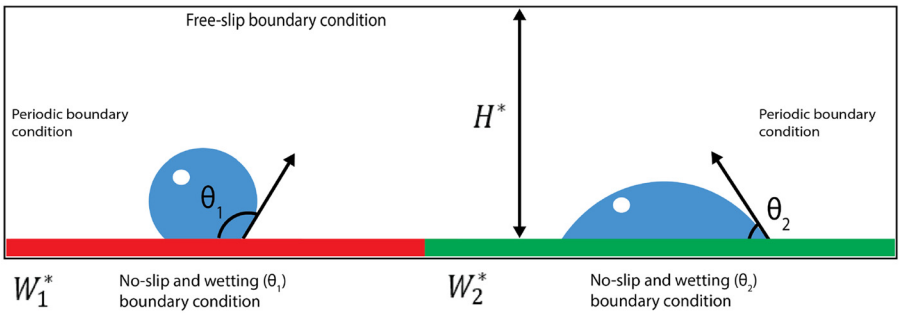

FIG. 2. Schematic of the simulation setup with a chemical step. The substrate is divided into a hydrophobic region (W_1^*, red) and a hydrophilic region (W_2^*, green), indicating a step change in the contact angle. The boundary conditions: periodic (left/right), no-slip and wetting (bottom), and free-slip (top).

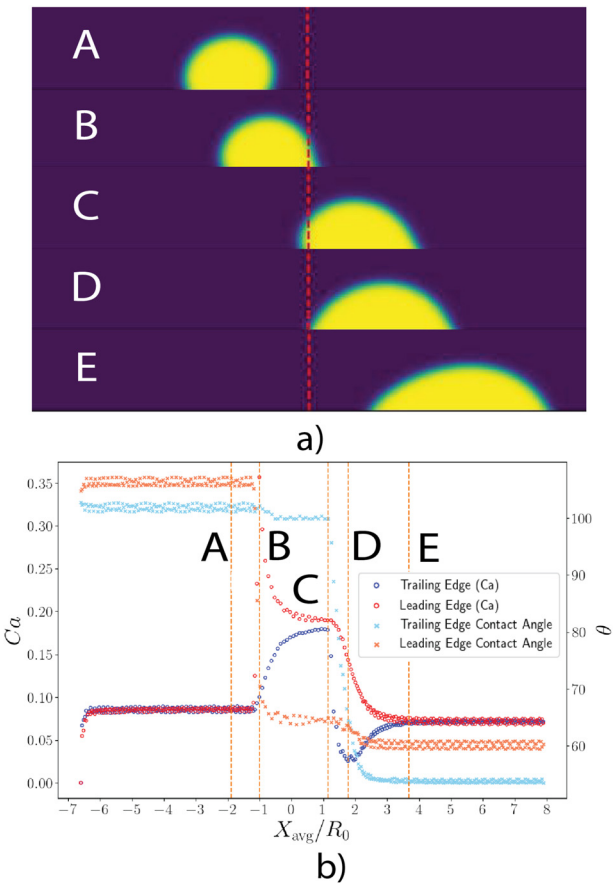

FIG. 3. Droplet dynamics over a chemical step. (a) Simulation snapshots labeled A–E, corresponding to the vertical orange dashed lines in (b): (A) pre-step steady state, (B) leading edge at the chemical step, (C) trailing edge at the step, (D) equal leading and trailing angles, (E) post-step steady state. (b) Evolution of the capillary number (Ca, left axis) and contact angle (θ, right axis) for the droplet's leading and trailing edge as functions of the normalized average X-location (X_{avg}/R_0). Here, the droplet velocity (v_d) in the capillary number is replaced by the velocities of the leading and trailing edge, which are determined by comparing the contact line locations (x_{cl}) between the current and previous time step, $v(t) = \frac{x_{cl}(t) - x_{cl}(t-\Delta t)}{\Delta t}$. Results are from a simulation with Bo $= 0.23$, $\alpha = 60^\circ$, the hydrophobic window is $\theta_A, \theta_R = [110^\circ, 100^\circ]$, and the hydrophilic window is $\theta_A, \theta_R = [60^\circ, 50^\circ]$.

hydrophilic CAH window. The simulation boundaries are periodic in the lateral direction, with no-slip and wetting conditions at the solid substrate and a free-slip condition at the top boundary. Since we focus on step dynamics, all simulations are terminated when the leading edge reaches 350 lattice units. Further details of the numerical method, including validation details, can be found in the supplementary material.

Figure 3(a) shows a series of snapshots taken from the simulation displaying the movement of the droplet down the inclined substrate, starting in the hydrophobic part, across the chemical step, and then down the hydrophilic part. Various moments in the series are annotated by the letters A to E. Figure 3(b) represents the corresponding plot of the droplet dynamics, denoted by the evolution of the capillary number ($Ca = \frac{\mu v_d}{\gamma}$, where μ is the dynamic viscosity, and v_d is the average velocity of the droplet) and the contact angle (θ) on the vertical axes and the dimensionless position (X_{avg}/R_0) on the horizontal axis. The moments A–E are also shown on this plot, and they correspond directly to the snapshots in Fig. 3(a). We notice that the droplet first accelerates (due to gravity) and then achieves a steady state velocity (denoted by Ca) on the hydrophobic side (moment A). At the moment (B), the leading edge of the droplet reaches the chemical step, we observe a deformation of the droplet, which results in a sharp increase in the velocity of the leading edge. In order to probe this sudden acceleration of the leading edge, let us consider the force balance on the droplet,

$$F_{\mathrm{x,droplet}} = mg \sin\alpha - w \cdot \gamma(\cos\theta_R - \cos\theta_A) - \lambda A v_{x,d}, \qquad (6)$$

where $F_{\mathrm{x,droplet}}$ is the total force acting on the droplet of mass m parallel to the incline, w is the width of the droplet perpendicular to the direction of motion, λ is a friction factor, A is the contact area of the droplet with the surface, and $v_{x,d}$ is the x-component velocity of the droplet.[31,32] The first term represents the gravitational force, the second term is the force due to the asymmetric contact angles (hysteresis force), and the last term accounts for the resistive viscous forces. The friction factor accounts for both the bulk and contact line contributions, both linear functions of velocity.[31] Force balance analysis reveals that for representative droplets, the viscous force dominates over the hysteresis force at steady state. This is consistent with recent spreading models, which have indicated that the contact-line contribution to viscous dissipation strongly influences droplet dynamics.[33] The friction factor is not specified in the numerical model but invoked to interpret the results. Finally, the two-dimensional droplet represents the

midplane of a symmetric three-dimensional droplet. Additional information on the force balance, including a scaling and worked out force balance analysis, are provided in the supplementary material.

As the leading edge reaches the chemical step, the contact angle of the leading edge reduces significantly. This is apparent from the contact angle evolution plot in Fig. 3(b). As a result, at moment B, the leading edge of the droplet has a (much) lower contact angle than that of the trailing edge. This gives rise to a negative numerical value for the expression $(\cos\theta_R - \cos\theta_A)$ in the hysteresis term. Hence, the hysteresis force, instead of inhibiting the influence of gravitational acceleration, aids it, giving rise to the sharp increase in the leading edge velocity.

This rapid increase is momentary; the leading edge subsequently decelerates, while the trailing edge velocity increases (Moment C). This can be explained by the fact that as the velocity of the leading edge increases, the friction force ($\lambda A v$) increases as well, bringing down the total force acting on the droplet, leading to its deceleration. Furthermore, the friction factor λ depends on multiple mechanisms, such as viscous dissipation near the three-phase contact line,[32] and the internal pressure resisting deformation due to the change in contact angle at the step. While the leading edge goes through this deceleration, the trailing edge shows an acceleration due to the internal pressure resisting deformation as mentioned above.

Subsequently, between Moment C and Moment D, both the leading edge and the trailing edge decelerate, following the mechanism described above. We notice that between Moment D and Moment E, the leading edge keeps on decelerating until it reaches a new steady state velocity. The trailing edge velocity, however, reaches a minimum at moment D, when the droplet deforms to match the hydrophilic hysteresis window and starts increasing again, finally stabilizing at the same steady state velocity as that of the leading edge (beyond E). This can be attributed to the sharp decrease in the contact angle for the trailing edge around Moment D, before stabilizing for the hydrophilic side.

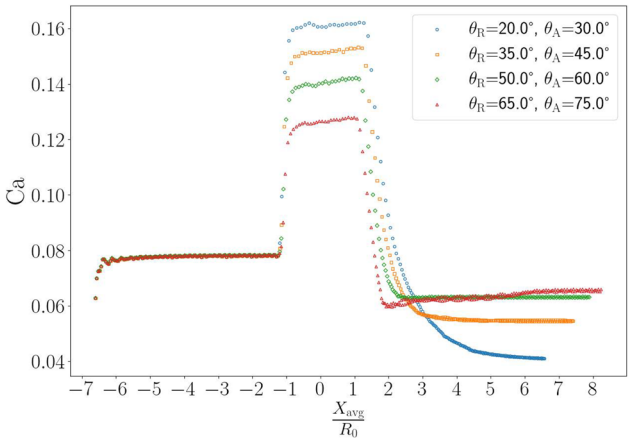

FIG. 4. Capillary number (Ca) as a function of normalized average *X*-location (X_{avg}/R_0) for simulations with different hydrophilic hysteresis windows (i.e., different θ_A and θ_R on the hydrophilic side of the step). The droplet velocity in the capillary number is taken as the average simulated velocity in the region $\rho > \frac{\rho_{l,1}+\rho_{l,2}}{2}$. Furthermore, the inclination angle is $\alpha = 60^\circ$, the hydrophobic window is $\theta_A, \theta_R = [110^\circ, 100^\circ]$ and Bo = 0.23, for all cases.

Having established that the leading and trailing edges of a droplet behave differently while crossing the chemical step on an inclined substrate, we now proceed to investigate the impact of the step strength on the overall dynamics. Figure 4 shows the capillary numbers (*Ca*) as a function of the normalized average *X*-location (X_{avg}/R_0) for various hydrophilic hysteresis windows. The hydrophobic hysteresis window remains the same in these simulations. We notice that as the hydrophilic hysteresis window contact angles decrease, i.e., as the difference between the characteristic contact angles on the hydrophobic and hydrophilic sides increases, the velocity of the droplet crossing the chemical step also increases. This is expected since the hysteresis force is stronger for a stronger chemical step (equivalent to the difference in the contact angles on the two sides of the step). In addition, a stronger chemical step leads to a larger deformation of the droplet, requiring more time to return to the stable shape. This is also evident from the time taken by these droplets to resume a steady state velocity.

In addition to the effect of hysteresis, the gravitational contribution to the force balance is significant. In order to investigate that contribution, we subsequently probed two parameters: (i) the angle of inclination (α) of the substrate and (ii) the volume of the droplet. During this investigation, the strength of the chemical step remains constant. Figure 5, which plots the modified capillary number ($\mathrm{Ca}/\sin\alpha$) as a function of the normalized average *X*-location, shows that relatively the jump in the velocity at the chemical step is the highest for the lowest α. The chemical step's effect on motion is set by the contact-angle change. We find that gravity dominates the droplet speed on either side of the step, while at all inclinations, the droplet's passage over the step is governed by contact angle hysteresis.

Finally, the volume of the droplet has been varied, reflected by the change in the characteristic *Bo* of the simulation. We notice in Fig. 6 that the droplets undergo different accelerations in the hydrophobic part of the substrate based on their volumes. They all experience a second jolt of acceleration as they enter the chemical step. The

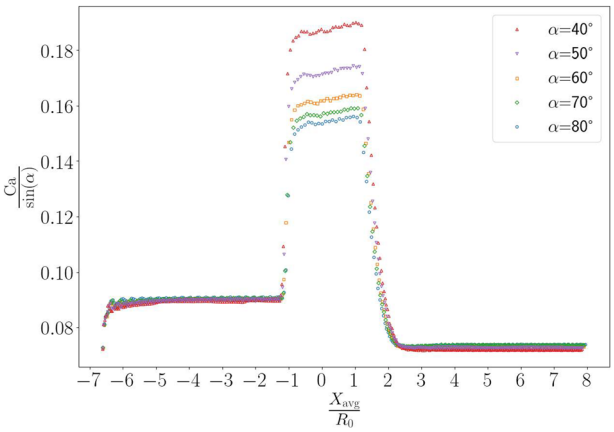

FIG. 5. Modified capillary number ($\mathrm{Ca}/\sin\alpha$) as a function of normalized average *X*-location (X_{avg}/R_0) for simulations where only the inclination angle α is varied. Furthermore, Bo = 0.23, the hydrophobic window is $\theta_A, \theta_R = [110^\circ, 100^\circ]$, and the hydrophilic window is $\theta_A, \theta_R = [60^\circ, 50^\circ]$, for all cases.

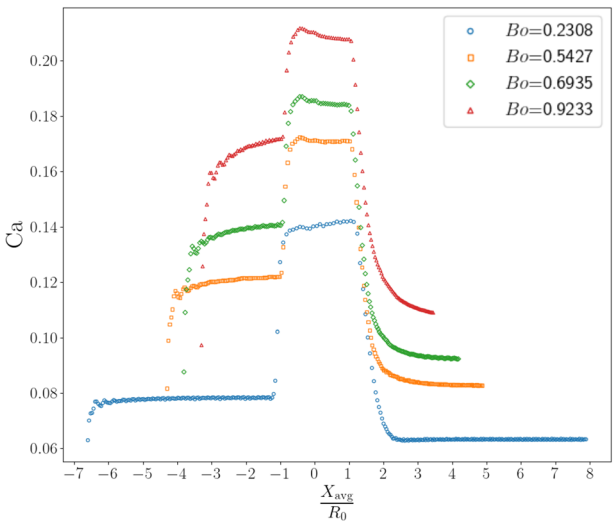

FIG. 6. Capillary number (Ca) as a function of normalized average *X*-location (X_{avg}/R_0) for simulations where only the radius of the initial droplet R_0 is varied, which alters *Bo*. Furthermore, the inclination angle is $\alpha = 60^\circ$, the hydrophobic window is $\theta_A, \theta_R = [110^\circ, 100^\circ]$, and the hydrophilic window is $\theta_A, \theta_R = [60^\circ, 50^\circ]$, for all cases.

relative jump in their velocities is inversely proportional to the volume of the droplet, as expected from the force balance. Moreover, the droplets with $Bo > 0.5$ undergo a mild deceleration since their larger absolute velocity increases the influence of the resistive viscous forces. This implies that for lower Bond numbers, hence for smaller droplets, the passing of the droplet over the chemical step is smoother than for larger droplets. For the larger droplets, they experience deformation due to the wettability change and, subsequently, the center of mass of the deformed droplet experiences a small deceleration while on the step. At the end of the step, the entire droplet experiences a sharp deceleration before approaching a steady state velocity. Note that for large *Bo*, the capillary number is already close to this post-step steady value, although the plateau is not fully developed within the simulated domain.

In conclusion, we have investigated the dynamics of a liquid droplet moving down an inclined substrate over a hydrophobic to hydrophilic chemical step, while the whole system is submerged in a liquid of lower (one-third) density than that of water. We implement contact angle hysteresis by adapting existing wetting boundary condition methods. We notice that the leading edge and the trailing edge of a droplet go through different dynamics at the step, which plays an important role in the subsequent deformation and steady state velocity of the drop. Furthermore, if the step strength is increased, then the maximum velocity attained during the transition over the chemical step increases as well. Finally, when we vary the inclination angle, we notice that the pre- and post-step motions are dominated by gravity, whereas the contact angle hysteresis force plays a crucial role in the motion over the step. This makes it possible to manipulate the droplet, e.g., to bring it to a desired steady state velocity using these wetting effects. The qualitative acceleration behavior reported is expected to persist also for higher density ratios (water–air) with possible quantitative changes in the velocity. Our work opens the door for more controlled experiments with such systems and poses the option of direct comparison between experiments and numerical investigations.

See the supplementary material for details of the lattice Boltzmann simulations as well as additional simulation data.

AUTHOR DECLARATIONS

Conflict of Interest

The authors have no conflicts to disclose.

Author Contributions

Sacha B. Szkudlarek: Formal analysis (equal); Investigation (lead); Methodology (lead); Software (lead); Writing – original draft (lead). **Orest Shardt:** Formal analysis (equal); Methodology (equal); Supervision (equal); Writing – review & editing (equal). **Chris R. Kleijn:** Formal analysis (equal); Supervision (supporting); Writing – review & editing (supporting). **Bijoy Bera:** Conceptualization (lead); Funding acquisition (lead); Supervision (lead); Writing – review & editing (lead).

DATA AVAILABILITY

The data that support the findings of this study are available from the corresponding author upon reasonable request.

REFERENCES

[1]P. Moazzam, H. Tavassoli, A. Razmjou, M. E. Warkiani, and M. Asadnia, Desalination **429**, 111 (2018).
[2]V. Sharma, H. Ali-Loytty, A. Koivikko, K. Yiannacou, K. Lahtonen, and V. Sariola, Langmuir **37**, 3370 (2021).
[3]M. Cao, J. Ju, K. Li, S. Dou, K. Liu, and L. Jiang, Adv. Funct. Mater. **24**, 3235 (2014).
[4]J. Xu, S. Xiu, Z. Lian, H. Yu, and J. Cao, Droplet **1**, 11 (2022).
[5]S. Feng, Q. Wang, Y. Xing, Y. Hou, and Y. Zheng, Adv. Mater. Interfaces **7**, 2000081 (2020).
[6]Z. Cai, F. Chen, Y. Tian, D. Zhang, Z. Lian, and M. Cao, Chem. Eng. J. **449**, 137831 (2022).
[7]R. Malinowski, I. P. Parkin, and G. Volpe, Chem. Soc. Rev. **49**, 7879 (2020).
[8]C. H. Ahn, J. W. Choi, G. Beaucage, J. Nevin, J. B. Lee, A. Puntambekar, and R. J. Y. Lee, Proc. IEEE **92**, 154 (2004).
[9]C. G. Koh, W. Tan, M. Zhao, A. J. Ricco, and Z. H. Fan, Anal. Chem. **75**, 4591 (2003).
[10]C. Semprebon and M. Brinkmann, Soft Matter **10**, 3325 (2014).
[11]M. Musterd, V. van Steijn, C. R. Kleijn, and M. T. Kreutzer, Phys. Rev. Lett. **113**, 066104 (2014).
[12]W. Barthlott and C. Neihuis, Ann Bot. **79**(6), 667–677 (1997).
[13]T. Onda, S. Shibuichi, N. Satoh, and K. Tsujii, Langmuir **12**, 2125 (1996).
[14]M. Tenjimbayashi and K. Manabe, Sci. Technol. Adv. Mater. **23**, 473 (2022).
[15]M. Borowko and T. Staszewski, Int. J. Mol. Sci. **25**, 4550 (2024).
[16]A. R. Parkeer and C. R. Lawrence, Nature **414**, 33–34 (2001).
[17]A. Cavalli, M. Musterd, and F. Mugele, Phys. Rev. E **91**, 023013 (2015).
[18]J. De Coninck, J. C. Fernandez Toledano, F. Dunlop, and T. Huillet, Phys. Rev. E **96**, 042804 (2017).
[19]I. Devic, J. M. Encarnacion Escobar, and D. Lohse, Langmuir **35**, 3880 (2019).
[20]Q. Li, Y. Liu, B. He, and B. Wen, Langmuir **39**, 14487 (2023).
[21]Z. Guo, Phys. Fluids **33**, 031709 (2021).
[22]Y. Yu, Q. Li, and R. Z. Huang, Phys. Rev. E **104**, 015303 (2021).
[23]X.-G. Zhong, Y.-S. Liu, Y.-C. Yao, B. He, and B.-H. Wen, Chin. Phys. B **32**, 054701 (2023).
[24]H. Ding and P. D. M. Spelt, J. Fluid Mech. **599**, 341–362 (2008).
[25]B. B. Kazemian and P. Cheng, Int. J. Heat Mass Transfer **186**, 122454 (2022).

[26]P. L. Bhatnagar, E. P. Gross, and M. Krook, Phys. Rev. **94**, 511 (1954).
[27]Y. H. Qian, D. D'Humières, and P. Lallemand, Europhys. Lett. **17**, 479 (1992).
[28]J. Bao and Z. Guo, Comput. Fluids **268**, 106106 (2024).
[29]M. R. Swift, E. Orlandini, W. R. Osborn, and J. M. Yeomans, Phys. Rev. E **54**, 5041 (1996).
[30]M. R. Swift, W. R. Osborn, and J. M. Yeomans, Phys. Rev. Lett. **75**, 830 (1995).
[31]D. J. C. M. 't Mannetje, C. U. Murade, D. van den Ende, and F. Mugele, Appl. Phys. Lett. **98**, 014102 (2011).
[32]H.-J. Butt, R. Berger, J. De Coninck, and R. Tadmor, Nat. Rev. Phys. **7**, 425–438 (2025).
[33]Y. T. Aksoy, P. Eneren, E. Koos, and M. R. Vetrano, Phys. Fluids **34**, 042106 (2022).